A comprehensive study of electrode compression effects in all vanadium redox flow batteries including locally resolved measurements

Ghimire, Purna C.; Bhattarai, Arjun; Schweiss, Rüdiger; Scherer, Günther G.; Wai, Nyunt; Yan, Qingyu

2018

Ghimire, P. C., Bhattarai, A., Schweiss, R., Scherer, G. G., Wai, N., & Yan, Q. (2018). A comprehensive study of electrode compression effects in all vanadium redox flow batteries including locally resolved measurements. Applied Energy, 230, 974-982. doi:10.1016/j.apenergy.2018.09.049

https://hdl.handle.net/10356/143309

https://doi.org/10.1016/j.apenergy.2018.09.049

A comprehensive study of electrode compression effects in all vanadium redox flow batteries including locally-resolved measurements

Purna C. Ghimire[1,2,[+]], Arjun Bhattarai[2,5,[+]] Rüdiger Schweiss[3], Günther G. Scherer[4], Nyunt Wai[2], Qingyu Yan*[5]

[1]*Interdisciplinary Graduate School, Nanyang Technological University, Singapore*

[2]*Energy Research Institute @Nanyang Technological University, Singapore*

[3]*SGL Carbon GmbH, Meitingen, Germany*

[4]*5607 Hägglingen, Switzerland*

[5]*School of Material Science and Engineering, Nanyang Technological University, Singapore*

[+] These authors contributed equally to this work.

Abstract

Graphite felts are the most commonly used electrode materials in vanadium redox flow batteries. In the conventional cell design, flat sheets of graphite bipolar plates and porous graphite felts are stacked without any bonding, which requires a certain degree of compression to minimize the contact resistance. Excessive compression of the electrode, however, leads to non-uniform flow distribution and potential occurrence of zones with retarded flow of electrolyte. In this study, we investigate a wide range of electrode compressions and their effect on the cell performance. In addition to conventional figures of merit, such as efficiencies and resistances, effects of electrode compression on pressure drop, flow distribution and SOC conversion are examined. Our results show that a compression of 25% is the optimal trade-off between contact resistance, flow distribution and pumping losses for the materials utilized in this investigation. At this compression level, spatially resolved measurements using a segmented cell show that optimal conversion of the reactants can be

achieved within a single pass. A relationship between change in SOC and flow distribution is also established.

Keywords

Vanadium redox flow battery; Electrode compression; Segmented cell; Local-voltage distribution; Flow distribution

1. Introduction

The vanadium redox flow battery (VRFB) has emerged as one of the most promising technologies for large-scale electricity storage. It offers unique characteristics, such as the ability to independently configure energy and power, absence of cross-contamination due to the use of the same metal ions in both electrolyte tanks, ambient temperature operation and long cycle life [1, 2]. The inevitable crossover of active species in flow batteries is not critical in the case of a VRFB since the use of species from a single element allows for an easy rebalance of the electrolyte.

Graphite felts electrodes are used in VRFB because of their three-dimensional structure, stability in acidic condition, high porosity (> 90%), high conductivity and large surface area. Moreover, these materials show high elasticity upon compression and thus do not require bonding to the current collector. Numerous studies have been conducted to improve the performance of VRFB components. Examples include thermal surface oxidation [3], chemical etching [4] and catalyst deposition [5-10] onto the porous graphite felt to enhance the electron transfer rate. Similarly, perforation or integration of channels into the electrodes to reduce the pressure drop [11, 12] , addition of chemicals to the electrolyte for the thermal stability [13], and design changes to lower the cell resistance have also been attempted.

In the conventional VRFB design, the cell frames accommodate the bipolar plates (BPs) and provide a cavity for the felt electrodes. The depth of the latter determines the compression

level of the felt adjacent to the BP. Compression of the felt electrode improves the electronic contact to the BP at the expense of a reduction in electrode porosity. Excessive compression, however, has several negative consequences, in particular it leads to a higher pressure drop. This is accompanied by higher pumping losses and non-uniform flow distribution of the electrolyte, which ultimately could lead to a reduction in electrode utilization and formation of dead zones (i.e. areas with less supply of fresh electrolyte). These effects are most critical during charging, as they could trigger elevated gas evolution and corrosive degradation of the BPs [14]. Therefore, optimization of electrode compression is a necessary task for optimal performance and longevity of flow battery stacks.

The pressure drop is another important parameter, which must be considered during the selection of the appropriate electrode compression. Energy consumed by pumping varies linearly with the differential pressure. The pressure drop (ΔP) occurs between flow inlet and outlet, due to the viscous resistance to flow, which is dependent on the viscosity of electrolyte and permeability of the porous electrode. For laminar flow, the pressure drop is given by Darcy's law

$$\Delta p = \frac{\eta_e}{K_e(\varepsilon)} \cdot Q \cdot \frac{L}{\varepsilon A} \tag{1}$$

Where η_e, Q, L, A, K_e, represent the viscosity of the electrolyte, the flow rate, the flow path length, the cross-sectional area of the felt and the permeability of the electrode (which is dependent on the porosity ε), respectively. During operation of a VRFB, the pump consumes about 1-3% of the total energy [2, 11], mostly due to the pressure drop across the porous electrodes. To reduce ΔP, several approaches, such as flow channels in the porous electrodes or in the BPs, have been proposed [11, 15].

To date, only a handful of studies have been performed towards understanding the influence of electrode compression on the overall performance of a VRFB. Park et al. [16] observed a

sharp decrease in specific resistance up to 10% of electrode compression and a flattening decline of resistance for higher levels of compression. Chang et al. [17] studied the change in electrical, morphological and mechanical properties up to a felt compression of 40%, using BPs containing flow channels. They showed that the increase in clamping force leads to a decrease in porosity underneath the rib and channel, which is attributed to the deformation of the carbon felt accompanied by a loss in void volume. In addition, to those experimental studies, several numerical approaches are available. For instance, Brown et al. [18] modelled the pressure drop in 3D microstructures using computational fluid dynamics. Likewise, the effect of electrode porosity on the charge/discharge behaviour [19] [20] and the pressure drop through the felt has also been modelled [21].

Overall, it appears that the focus of previous studies on electrode compression is on the electronic resistance and the efficiency. However, less attention is paid to the effect of compression on flow distribution and electrolyte utilization. We believe that the discharge energy, which is lacking in most of the published reports, will be a more meaningful figure of merit for the characterization of the effects brought about by electrode compression. Moreover, most of the experimental studies have been performed using either a fuel cell design (with thin electrodes and BP with flow fields) or a cell with small active area. The effect of non-uniformity and change in contact resistance may rather be prominent in cells with larger dimensions.

Hence, this study investigates the effect of carbon felt compression on electronic conductivity, pressure drop in both half-cells and overall cell performance during charging and discharging in a 100 cm^2 VRFB cell. In addition, local OCV mapping is performed to study the effect of cell compression on the electrode utilization at three different compression levels, using a segmented cell approach.

2. Experimental

An in-house developed flow cell with an active area of 100 cm^2 (10 cm x 10 cm) was employed. The arrangement of the different components is shown in Figure S1. The PVC flow frames were provided with flow guides to facilitate uniform flow of electrolyte through the porous electrode. Stainless steel plates (10 mm thick) were used as end plates for pressing the components into contact. Copper plates were selected as current collectors. Battery-grade polyacrylonitrile (PAN)-based carbon felts (Sigracell® GFD, 6 mm thick, SGL Carbon GmbH, Meitingen, Germany) were employed as electrodes. Felts were thermally activated in air at 600°C for 5 hours. The cell was assembled with Sigracell® TF6 graphite BPs (SGL Technic LLV, Valencia, CA, USA) and an anion exchange membrane (FAP 450, Fumatech GmbH, Bietigheim-Bissingen, Germany).

Six different compression levels of the porous electrode (15%, 20%, 25%, 30% 35% and 40%) were investigated. The electrode compression was varied by using combinations of silicone and Teflon™ gaskets of different thickness. A torque wrench was employed to ensure uniform compression of the electrode. After each assembly, the thickness between the two end plates was measured to ensure the exact compression of the electrode. The volume of the electrolyte in each tank was 150 mL and the concentration of the electrolyte was 1.6 M $V^{+3.5}$ in total 4.5 M sulfate (GFE, Nürnberg, Germany). The electrolyte flow rate in both half-cells was kept constant at 100 mL min^{-1} by means of peristaltic pumps. Nitrogen at a flow rate of 10 mL min^{-1} was supplied routinely to both electrolyte tanks to maintain an inert atmosphere in the headspace of the electrolyte. The pressure drop in each half-cell was continuously measured using two pressure gauges (Georg Fischer, Germany). Similarly, the temperature was continuously monitored in both the tanks by PT100 type sensors.

An identical cell was assembled without ion-exchange membrane to determine the dry cell resistance by means of the four-probe method. Cell cycling was performed using a battery

charger (NEWARE, China, 10 V, 10 A). Five cycles were run at varying current densities between 40 to 80 mA cm^{-2}, followed by 50 long term cycles at 40 mA cm^{-2}. Galvanostatic charge and discharge cycles were conducted between cut-off voltages of 1.65 V and 0.9 V, respectively.

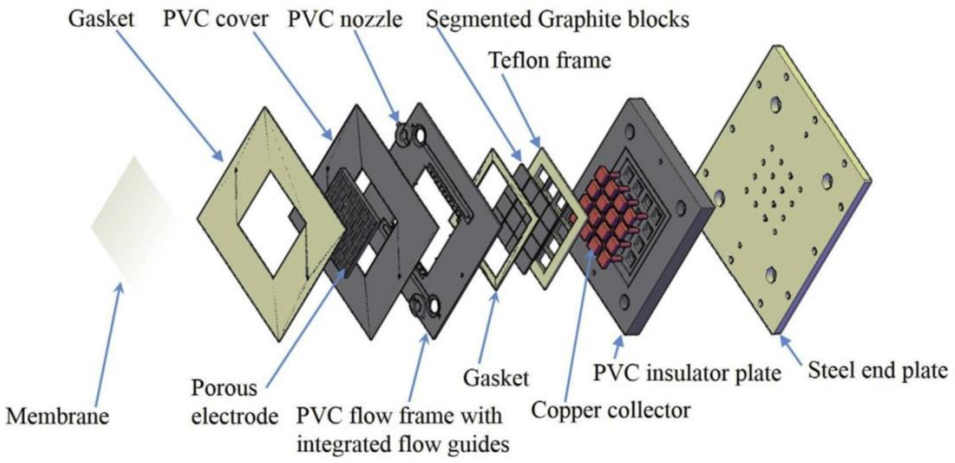

Figure 1: Exploded view of a VRFB single cell with segmented negative half-cell [14].

A segmented cell was designed for locally-resolved measurements. The bipolar plate of the negative electrode of a 100 cm^2 (10 cm x 10 cm) active area cell was divided into 16 segments, as shown in Figure 1. Segments were fabricated using graphite blocks (PVDF-bonded, F100 type, SGL Carbon GmbH, Meitingen, Germany), which were embedded into a PTFE frame. Each of them was attached to a copper current collector. Contacts to the battery tester were made by banana plugs through holes in the PVC insulator plates. The segmented cell study was performed for three compressions levels: 15%, 25%, and 40%. The volume of the electrolyte in each tank was 200 mL with 0.8 M $V^{+3.5}$ in total 4.5 M sulfate concentration. The low concentration of vanadium of 0.8 M was chosen deliberately in order to be able to operate in the mass transport regime at relatively low current densities. Flow rates were varied between 25 mL min^{-1} and 60 mL min^{-1} using peristaltic pumps. A battery tester (NEWARE, China, 5 V, 3 A), consisting of 16 terminals, was used to charge/discharge each segment. Since the segmentation was performed on the negative side, each negative segment

was connected to an individual channel of the battery tester, whereas all positive terminals of the battery tester were shunted together and connected to the positive half of the cell.

Figure 2 shows the picture of the segmented side with banana plug cables connected and the position of sixteen segments in the active area. As the flow was maintained in the upward direction, the segments (1-4) represent the inlet segments, whereas the segments (13-16) correspond to the outlet segments. The flow of electrolyte was through the cross-section of the (undivided) porous electrode. Flow guides in the frame ensured uniform entry of electrolyte into the porous electrode.

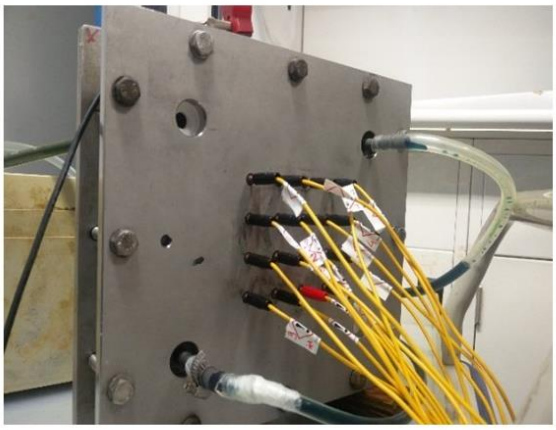

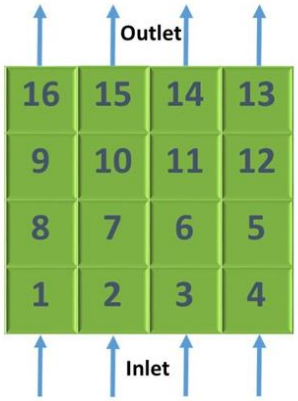

Figure 2: Segments at the negative half-cell (left) and position of 16 segments with flow direction of electrolyte (right).

The electrolyte was initially charged to 50% state of charge. Afterwards, the cell was kept at open circuit voltage (OCV) for 5 minutes, until all segments showed an identical OCV. Thereafter, cells were discharged for 1 min at 150 mA cm^{-2} using a flow rate of 60 mL min^{-1}. Finally, the cell was again switched to OCV for 5 minutes, until all segments were equilibrated. The same procedure was carried out at a flow rate of 25 mL min^{-1}. The OCV values obtained 5s after the termination of discharge were plotted into a contour diagram and were compared for different compression levels. The benefits of the use of OCV contour,

rather than discharge or charging voltage/current contours, are discussed in our previous work [14].

3. Results and discussion

3.1 Cell performance at different current densities

Figures 3a-d compare the coulombic efficiency (CE), energy efficiency (EE), voltage efficiency (VE) and specific capacity (in Ah L^{-1}) at six different levels of electrode compression, respectively.

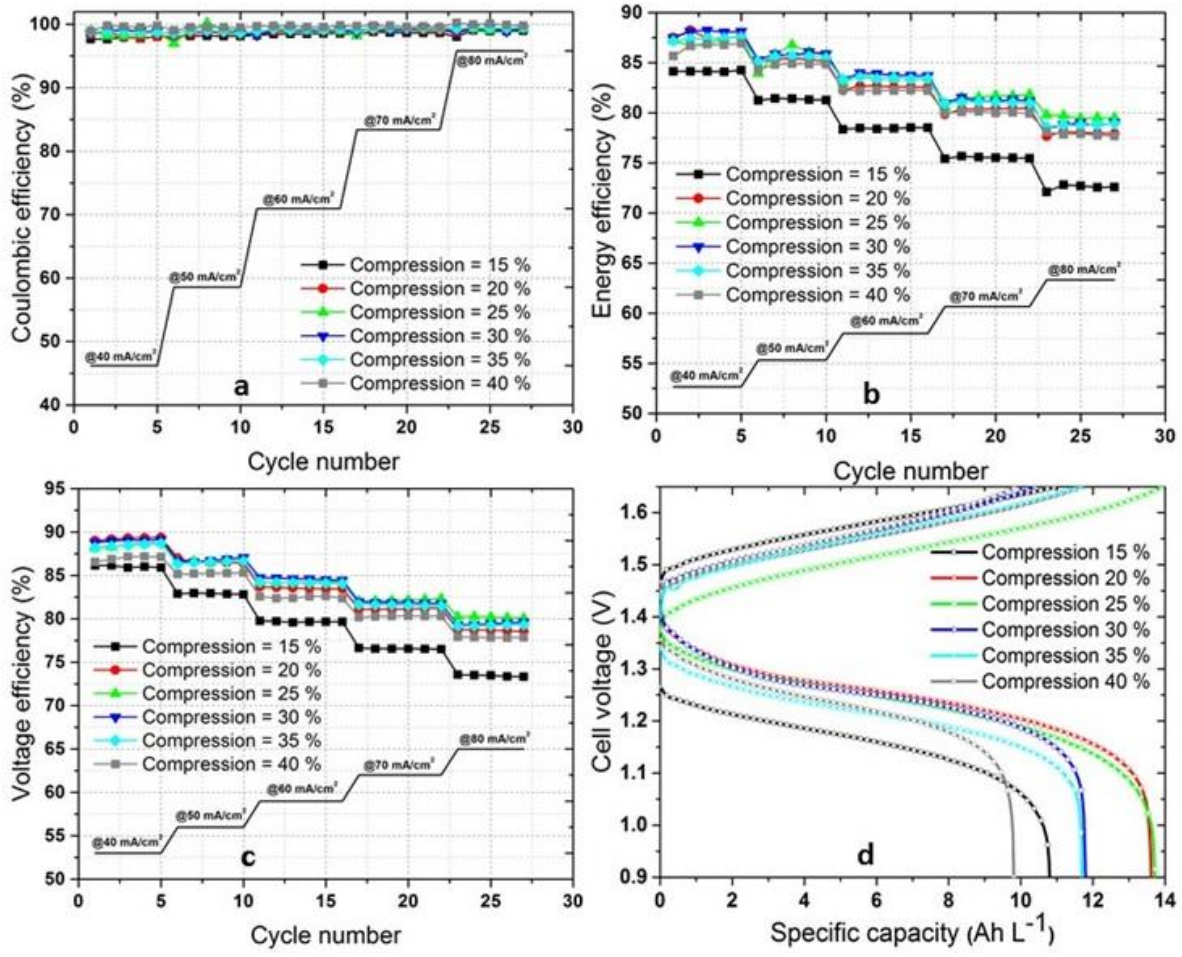

Figure 3: Comparision of: (a) coulombic efficiency, (b) energy efficiency, (c) voltage efficiency and (d) specific capacity at 80 mA cm^{-2} for different electrode compression levels.

The CE remained unchanged and nearly 100%, irrespective of the electrode compression. This is expected since the CE is dominated by the properties of the membrane. The VE and EE at 15% electrode compression were significantly lower compared to higher compressions. The inferior performance at 15% compression is attributed to a higher contact resistance. For comparison purposes, the 'dry' cell resistance was measured for various settings (Table 1).

Table 1: Electronic resistance of 'dry' cells (w/o membrane) at various electrode compressions.

Electrode compression (%)	15	20	25	30	35	40
Electronic area resistance (Ω cm^2)	1.1	0.78	0.75	0.72	0.61	0.58

As expected, the increase in the compression of the electrode resulted in a decrease in Ohmic resistance. A closer look at the six different compression values revealed a sharp drop of the electronic resistance between 15% and 20%, followed by a small reduction in contact resistance with further increase in electrode compression. The observed trend is in good agreement with a previous study [16]. Hence, the poor energy and voltage efficiency at a value of 15% electrode compression were predominantly caused by poor interfacial contact between the felt and the BP. The highest EE and VE were found for an electrode compression between 25% and 30%. This could be an indication that the cell performance cannot be improved by a reduction in contact resistance alone. At higher current densities effects of mass transport need to be considered.

Figure 3d shows the charge/discharge profile at a current density of 80 mA cm^{-2} for different electrode compression values. The potential drop was highest for 15% of electrode compression. As the compression increases, the IR losses in the corresponding charge and discharge cycles are reduced. When both, the resistance and the specific capacity, are taken

into account, the optimal trade-off between electrolyte utilization and contact resistance is exhibited by the electrode compressed at a value of 25%.

3.2 Cell performance at a current density of 40 mA cm^{-2} in long term cycling

To scrutinize the effects on long term cell performance, fifty cycles were run at current density of 40 mA cm^{-2}. The energy efficiency (EE) and discharge energy (DE) at various electrode compressions are compared in Fig. 4a and 4b, respectively.

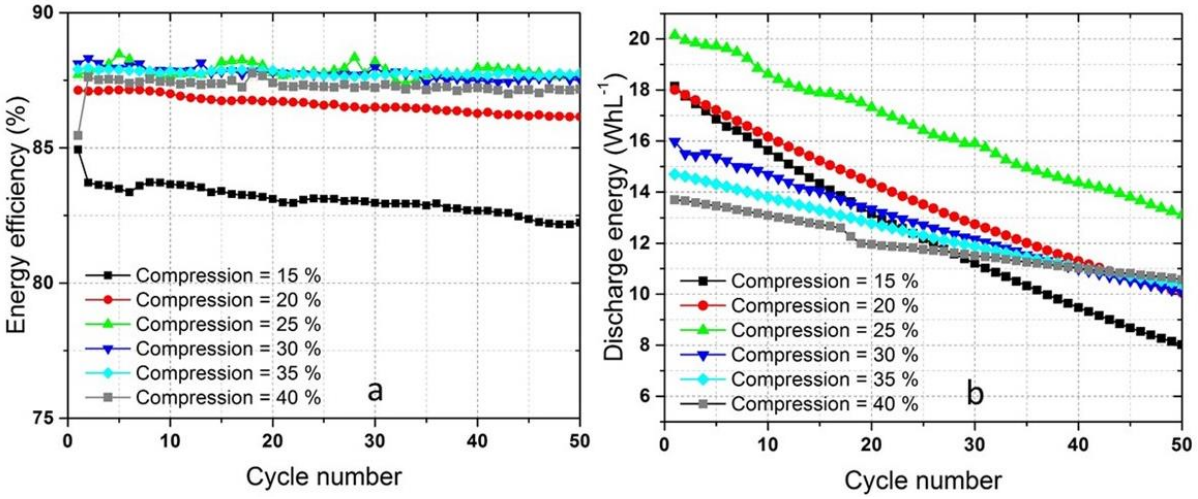

Figure 4: (a) Energy efficiency and (b) discharge energy during 50 cycles at 40 mA cm^{-2}.

A nearly stable EE with was observed at all compressions during long term testing. The small decrease in EE was attributed to the well-known electrolyte imbalance, which evolves over time. The maximum EE was obtained with cells employing an electrode compression between 25% and 30%. By contrast, the highest drop in EE and capacity of 4% over 50 cycles were observed for the cell with an electrode compression value of 15%. Since the cells were operated at constant voltage cut-off mode, the discharge capacity (Ah) and discharge energy (Wh) showed a very similar pattern. Interestingly, the decay rate of discharge energy (Wh) and discharge capacity (Ah) was a function of electrode compression. The discharge capacity decay over 50 cycles is shown in Table 2.

Table 2: Discharge capacity decay (%) for different compressions over 50 cycles.

Compression (%)	15	20	25	30	35	40
Discharge capacity decay (%)	55	44	36	35	29	23

As shown in Figure 4b, an electrode compression by 25% exhibits the best initial DE and the highest retention over 50 cycles. This reflects the optimum trade-off between contact resistance and electrolyte utilization. The capacity fade (Figure 4b) was reversible, since the capacity drop and the EE were recovered after rebalancing of the electrolyte. This indicates that the capacity fade is solely due to electrolyte crossover. As evident from Table 2, the discharge capacity was reduced when the electrode compression was increased. A likely reason could be a larger number of dead zones on the electrode and membrane, which increased with the electrode compression. This resulted in lower electrolyte crossover through the reduced active membrane area. A similar trend was also observed in a previous work [16]. Another explanation for the capacity reduction could be given by a variation in differential pressure between the two half-cells. At a fixed flow rate, the pressure drop between flow inlet and outlet is higher at the negative side, as shown in Figure 6. In addition, the pressure difference between two half-cells may arise for a higher electrode compression levels. The net transfer of electrolyte in VRFB cells using AEMs due to electro-osmotic drag is from the positive side to the negative side. Hence, convective transfer due to a difference in pressure drop may act in opposite direction to the electro-osmotic transfer direction, possibly resulting in the decrease of a capacity decay with an increase in electrode compression.

As the flow through the porous electrode is assumed to be laminar (Re =0.09), the viscous resistance will be dominant. The (average) permeability at various electrode compressions was calculated (Table 3) using the data sheet provided by the manufacturer [22]. The viscous

resistance, which is an indication of resistance to liquid flow, was calculated by reciprocating the permeability.

Table 3: Permeability, viscous resistance and porosity change at different levels of electrode compression.

Electrode compression (%)	**0**	**15**	**20**	**25**	**30**	**35**	**40**
Average permeability ($10^{-11}m^2$)	11	7	6.25	6	5.5	5	4.9
Viscous resistance ($10^{10}m^{-2}$)	0.91	1.43	1.6	1.67	1.82	2.0	2.04
Increase in viscous resistance (%)	0	57	75	84	100	120	124
Porosity (%)	92	90.6	90	89.3	88.5	87.7	86.6

The change in porosity with an increase in electrode compression is given by

$$\varepsilon = 1 - \frac{h_0}{h}.(1 - \varepsilon_0) \quad (2)$$

Where h_0, h, ε_o, ε represent the initial thickness, compressed thickness, porosity before compression and porosity of the compressed felt, respectively.

Summarizing the values exhibited in Table 1 and 3, it is evident that at lower compression values (< 20%), the contact resistance was higher and the flow distribution can be assumed to be more homogeneous, as a result of a higher permeability. With the increase in compression, the electronic contact resistance was reduced, whilst the viscous resistance increased significantly. At 40% electrode compression, the low values of discharge energy and discharge capacity reflect the fact that the electrolyte was not fully utilized. This is because the overpotential increased owing to poor flow distribution across the porous electrode.

3.2 Change in internal cell resistance (R_i)

The internal resistance is a parameter that can be used to compare the different cell designs. The internal resistance of the flow cell during charging and discharging can be calculated via

$$R_t = \frac{V_{oc}}{j} \cdot \frac{(1-VE)}{(1+VE)} \tag{3}$$

Where R_i, V_{oc}, j and VE represent the average (area-specific) internal resistance (Ω cm^2), average open circuit voltage during charging and discharging (~ 1.38 V at 25°C), the current density (A cm^{-2}) and the voltage efficiency, respectively. Figure 5a summarizes the internal resistance at different current densities for cells assembled with different electrode compression levels. The internal resistance decreased at an electrode compression up to a value of 25% and increased slightly with further increment. This behaviour points at a loss of elasticity of the felt, caused by over-compression. A similar trend was observed during long term cycling at 40 mAcm^{-2}, as shown in Figure 5b. A small increment in R_i with cycling was due to a decrease in EE as an effect of electrolyte crossover.

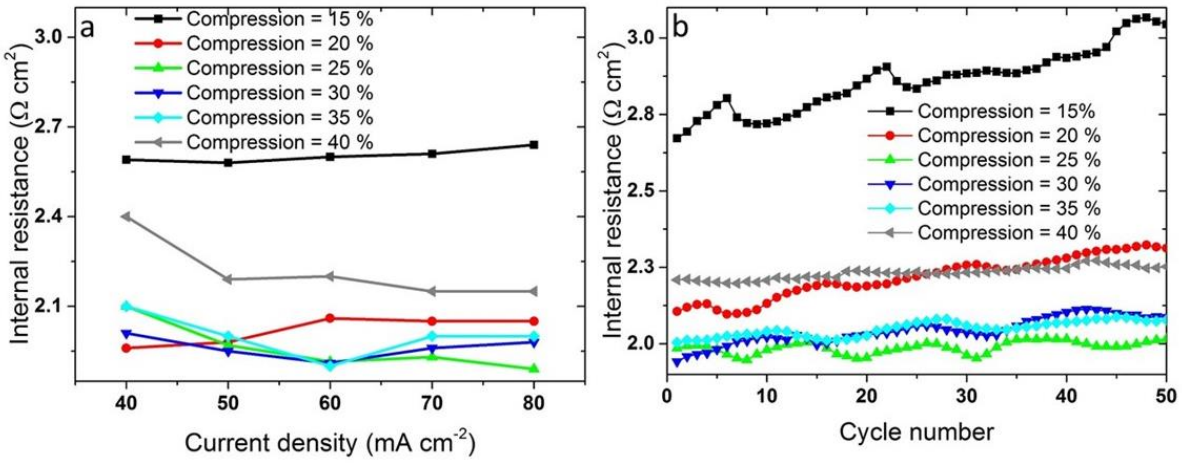

Figure 5: Internal resistance for various compressed electrodes (a) at different current densities and (b) at 40 mA cm^{-2} for 50 cycles.

The combined membrane and charge transfer resistances as well as concentration change in cell can be estimated by subtracting the value of the dry cell resistance from the value of the wet cell resistance. The values obtained at 80 mA cm^{-2} for 15%, 20%, 25%, 20%, 35% and 40% of electrode compression were 1.54, 1.27, 1.14, 1.25, 1.39 and 1.56 Ohm cm^2, respectively. This indicates that cells with uniform flow distribution utilize the electrode and membrane area more effectively. This results in a lower difference in dry/wet resistances, as observed for the electrode compressed at 25% and 30%. The value for the membrane resistance alone is around 0.7 $Ohm.cm^2$, as stated in the corresponding data sheet of the manufacturer [23].

3.4 Effect of compression on pressure drop (ΔP)

The value of the pressure drop ΔP for both, the positive and the negative half-cell, for the first five cycles are compared in Fig 6a and 6b. Initially, the positive and negative electrolyte containers were filled with electrolyte containing the same composition of vanadium species ($V^{+3.5}$). A sinusoidal oscillation in pressure drop in both the half-cells occurs during cell cycling, because of the continuous change in viscosity of the electrolyte. The viscosity was highest at the negative side during discharge and lowest at fully charged condition. In comparison to the negative half-cell, the change in ΔP on the positive half-cell was not significant, since the variation in viscosity during charging/discharging is low.

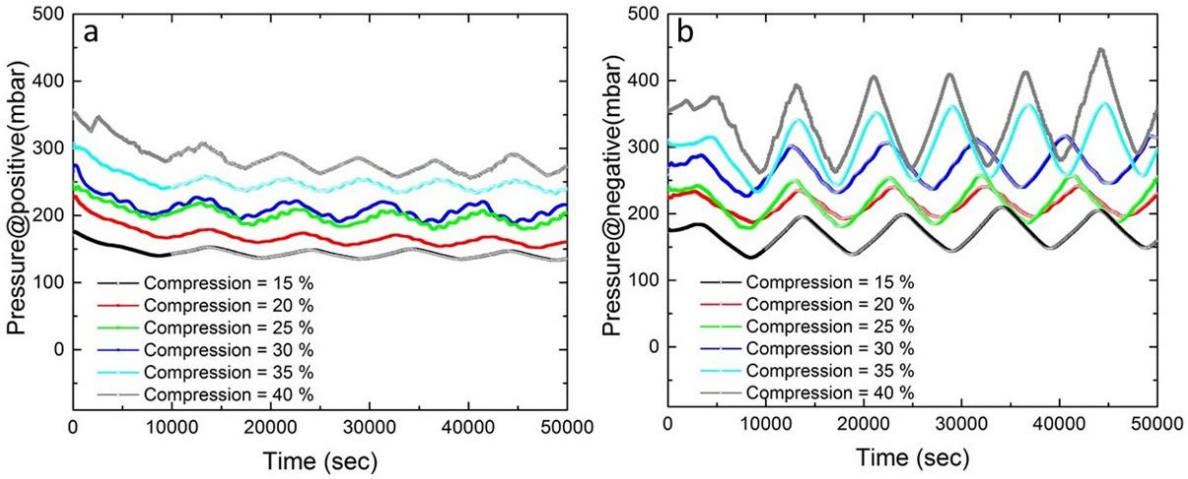

Figure 6: Pressure drop in (a) positive half- cell and (b) negative half-cell.

A significant increase in pressure drop (ΔP) was recorded when the electrode compression was increased. As the pumping energy is directly proportional to ΔP, the increase in pressure drop increases the parasitic loss associated with pumping. During complete charging and discharging, the full change in ΔP in the negative half-cell was 187 mbar for a value of 40% electrode compression, whereas it was only 73 mbar for a value of 25% compression. Moreover, the difference in pressure between the two half-cells at 40% electrode compression was about 107 mbar, while it was reduced to 43 mbar at 25% of compression. Such reduced pressure difference between two half-cells also lowers the convective drag. This results in a lower electrolyte crossover [24].

3.5 Effect of pumping loss on the overall energy efficiency

Assuming a pumping efficiency of 0.7, the required pumping power for a specific (volumetric) flow rate (Q) was estimated to

$$P_p = 2 \cdot \frac{\Delta P.Q}{0.7} \tag{4}$$

Where, P_p is the pump power (Watt) and Δp is the pressure drop (Pa). The power consumption was calculated for two pumps. The pressure drop caused by bends, manifolds

and pipes was deemed to be negligible as compared to the Δp across the porous electrode. For simplification, an average of the pressure drop from the two half-cells was used. Fig. S2 shows the pressure drop (in mbar) and consumed pumping power (in mW) for the different electrode compressions.

Figure 7 shows the overall EE with (a) and without consideration of pumping losses (b) for different compression levels.

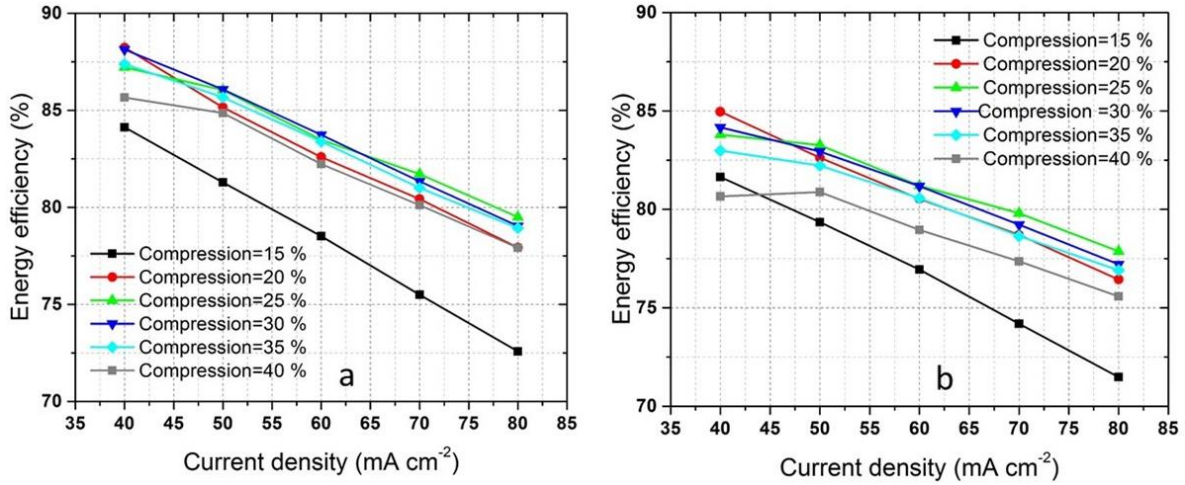

Figure 7: Energy efficiency (a: Net EE excluding pump power consumption and b: EE including pump power consumption) of VRFB cells at different current densities and compression levels.

Taking the total pump energy consumption into consideration (Figure 7b), the highest efficiency was achieved for an electrode compression of 25%. For instance, comparing 25% compression against 15% compression, the maximum improvement on EE at 25% compression was 2.4% and 6.4% at 40 and 80 mA cm^{-2}, respectively. Similarly, comparing 25% compression against 40% compression, an improvement of 3.1% and 2.3% of EE at 25% compression was obtained at 40 and 80 mA cm^{-2}, respectively. The effect of pumping losses on the EE at 25% compression, which is found to be optimal among all compression levels, was calculated to be 3.4% at 40 mA cm^{-2} and 1.6% at 80 mA cm^{-2}.

3.6 Spatially-resolved OCV distribution at different compression levels

A segmented cell approach was used to investigate the effect of electrode compression on the flow distribution. Accordingly, cells were assembled at high, medium and low compression (40%, 25% and 15%, respectively). The electrolyte concentration of 0.8 M at 25 mL min^{-1} and 60 mL min^{-1} corresponds to a stoichiometry value (λ) of 1 and 2.5, respectively. The latter is calculated from Faraday's law:

$$\lambda = \frac{Q_{app}}{Q_{st}} = Q_{app} \cdot \frac{nF \cdot c_V \cdot SoC}{I} \quad (5)$$

Where, Q_{app} is the applied flow rate, Q_{st} the stoichiometric flow rate at specific current density, I the total current, SOC the state of charge (0.5), c_V the total concentration of the vanadium ions in mol L^{-1}, n the number of electrons involved (here n = 1) and F is Faraday's constant (96485 As mol^{-1}).

In our previous study [14], we established a method to study the flow distribution by analysing the open circuit voltage (OCV) immediately after terminating the charge or discharge process, as the distribution of OCV reflects the charged species status in the electrode during current flow. As the OCV is unaffected by the variation in the resistance value in between the different segments of the cell, it is very effective to study the flow distribution using the OCV contours. Additionally, the OCV can be converted to the corresponding SOC for ease of interpretation, thereby making it very useful for the explanation of the flow behaviour at different electrode compression.

During charging and discharging, an OCV difference between inlet to outlet of the segment was observed, due to conversion of redox species. When the OCV was monitored at 5s after termination of the discharge process, flattening of the OCV also occurred between inlet to outlet on the contour diagram, as the OCV reflected the status during the discharge with

minimal drift. Since the temporal resolution of the battery tester is around 1s, the OCV data after 5s of discharge was found to be a solid compromise, which avoids measurement noise and provides a smooth OCV profile [14].

In order to investigate the utilization of the electrode during discharge at high current density at three different electrode compression levels, the experimental SOC change (ΔSOC_{exp}) was compared with the theoretical ΔSOC during a single pass of electrolyte. The theoretical SOC change (ΔSOC_{th}) is calculated using Faraday's law:

$$\Delta SOC_{th} = \frac{I}{(Q_{app} \cdot c_V \cdot F)} \tag{6}$$

Where, ΔSOC represents the change in state of charge between inlet to outlet in a single pass, and ΔSOC_{exp} was determined by taking the difference between the electrolyte SOC at inlet to the cell (i.e. at the inlet tube or tank) and at the outlet segments (i.e. lowest value in the SOC contour). Figure 8 shows the OCV contours at 5s after the termination of discharge at current density of 150 mA cm^{-2} for three electrode compressions. The plots from top to bottom represent the contour with an increase in electrode compression, whereas the left and right contours were plotted for measurements at the flow rates of 25 and 60 mL min^{-1}, respectively.

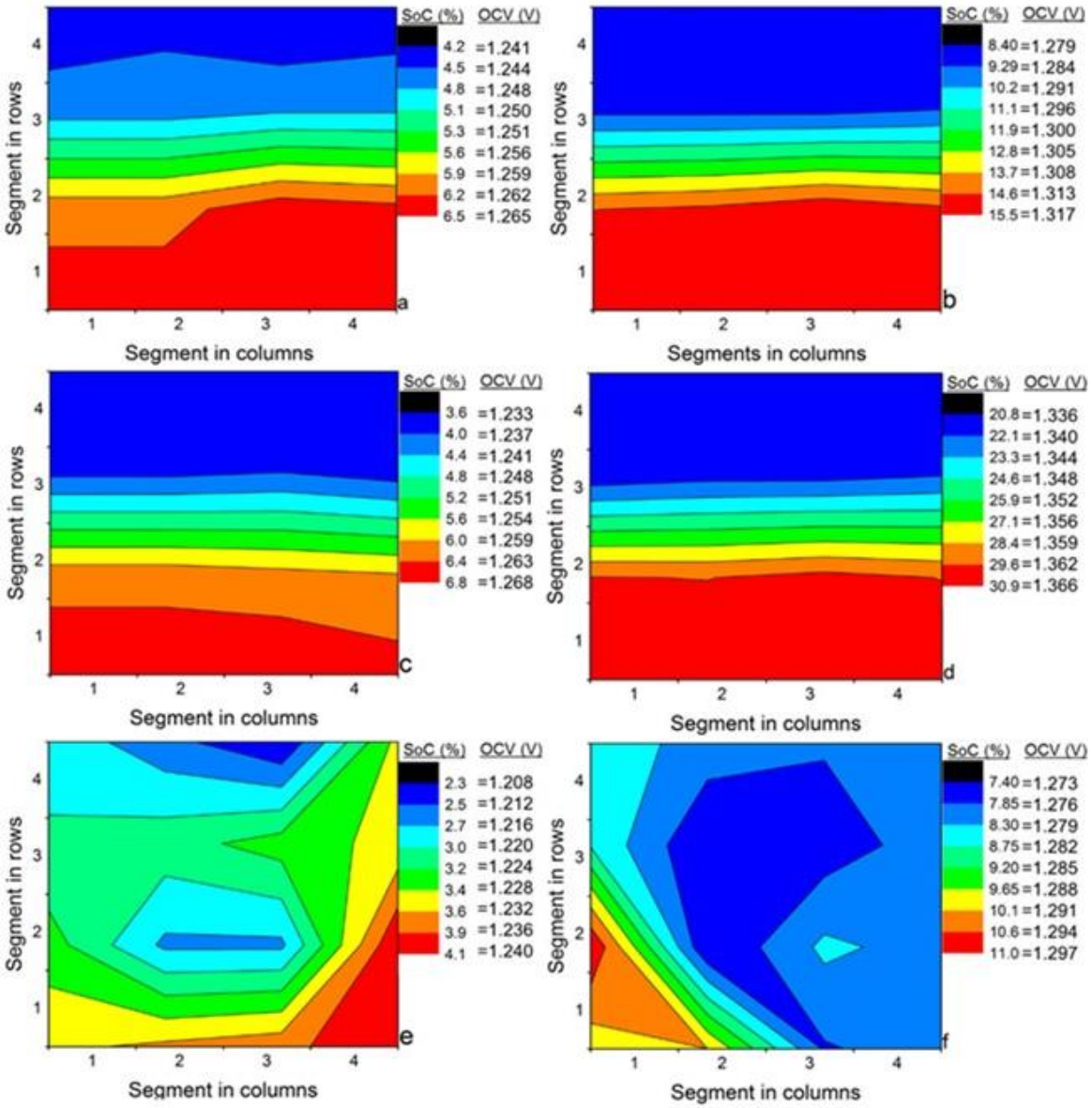

Figure 8: SOC (with corresponding OCV on the legend) contours for electrode compressed at 15%, 25% and 40% (top to bottom) measured at two flow rates (left contours @ 25 mL min^{-1} and right contours @ 60 mL min^{-1}). All the contours were measured 5s after the termination of discharge at 150 mA cm^{-2}.

If the OCV was measured immediately after terminating the discharge process, a higher voltage at the inlet segment and lower voltage at the outlet segment is expected, as the

charged species are depleted in the direction of flow. For a highly uniform flow distribution, a flat (band-like) distribution of the voltage along the cross-section of the flow. As revealed in Figure 8 a-d, a uniform band of SOC (or OCV) along the cross section of the electrode was observed for the compression of 15% (a and b) and 25% (c and d) at both flow rates of 25 mL min^{-1} (a and c) and 60 mL min^{-1} (b and d). However, when the electrode compression was increased to 40%, the SOC patterns indicate a non-uniform flow distribution. Again, this reflects the fact that a higher electrode compression decreases the porosity (probably non-uniform change in porosity in a thick felt of large area), resulting in the flow of electrolyte through a particular section of the electrode or even short-circuiting of the electrolyte. Therefore, a high voltage (or SOC) band appears in the area with access to electrolyte flow, whereas a low voltage band appears in the area with depleted reactants. The SOC contour also depicts the utilization of electrolyte along the flow path. In other words, the distribution of the electrolyte through the porous electrode can be quantified from monitoring the ΔSOC.

The deviation between theoretical and experimental ΔSOC describes different situations:

(i) Experimental ΔSOC ≈ Theoretical ΔSOC: Optimum utilization of electrolyte and excellent flow distribution

(ii) Experimental ΔSOC > Theoretical ΔSOC: Poor utilization (higher overpotential either due to over-discharge at the retarded/stagnant zone or higher contact resistance).

(iii) Experimental ΔSOC < Theoretical ΔSOC: Insufficient availability of redox species to sustain the applied current in the segments/electrode

Table 4 shows a comparison of the theoretical and experimentally determined ΔSOC during a single pass at stoichiometry values of λ=1 and λ=2.5, respectively.

Table 4: Theoretical and experimental conversion (SOC change) for different electrode compressions for cases shown in Figure 8.

Electrode compression	**Δ SOC (60 mL min^{-1}, λ=2.5)**	**Δ SOC (25 mL min^{-1}, λ=1.0)**
Theoretical	*19.43%*	*46.66%*
15%	30.09%	38. 93%
25%	20.9%	38.55%
40%	37.82%	40.98%

At a low flow rate of 25 mL min^{-1}, the experimental ΔSOC (ΔSOC_{exp}) value was found to be lower than the theoretical ΔSOC (ΔSOC_{th}). This is an indication that the segments near the outlet could not sustain the current for a long period during discharge, as previously reported in literature [14]. At high flow rate (60 mL min^{-1}), the experimental and theoretical ΔSOC matched closely for 25% compression. This indicates that the electrolyte conversion in a single pass occurred at the predicted rate. At a value of 15% compression, the contact resistance was higher compared to other compression values, resulting in a higher SOC difference between the inlet the outlet. Therefore, the value of the ΔSOC_{exp} was much higher than the value of the ΔSOC_{th}. At 40% compression, the electrolyte fully discharged at the location where the electrolyte was trapped, or stagnant or retarded flow occurred within the porous electrode. This again resulted in a higher ΔSOC value measured than the theoretical one expected. From the segmented cell approach, it becomes clear that a value of 25% electrode compression is an optimal trade-off between minimizing the contact resistance and maximizing the flow distribution.

4. Conclusions

A systematic study of the effects of electrode compression on all relevant performance parameters of VRFB has been carried out. The compression of the carbon felt electrodes was varied between 15% and 40% in VRFB cells with an active area of 100 cm^2. In addition to conventional figures of merit, such as efficiencies and resistances, effects of compression on the pressure drop and the flow distribution were investigated. The latter was visualized by means of locally-resolved measurements using the segmented cell approach. All the different experiments provide evidence that the utilized carbon felt electrodes compressed at 25% (with respect to the original thickness) constitute the optimum level, ensuring low contact resistances, moderate pressure drops, and homogeneous flow distribution across the porous electrode.

Acknowledgement

This research was financially and technically supported by Nanyang Technological University, Singapore, and SGL Carbon GmbH, Germany.

References:

[1] P. Alotto, M. Guarnieri, and F. Moro, "Redox flow batteries for the storage of renewable energy: A review," *Renew. Sustain. Energy Rev.*, vol. 29, pp. 325-335, 2014.

[2] A. Parasuraman, T. M. Lim, C. Menictas, and M. Skyllas-Kazacos, "Review of material research and development for vanadium redox flow battery applications," *Electrochim. Acta*, vol. 101, pp. 27-40, 2013.

[3] B. Sun and M. Skyllas-Kazacos, "Modification of graphite electrode materials for vanadium redox flow battery application—I. Thermal treatment," *Electrochim. Acta,* vol. 37, pp. 1253-1260, 1992.

[4] B. Sun and M. Skyllas-Kazacos, "Chemical modification of graphite electrode materials for vanadium redox flow battery application—part II. Acid treatments," *Electrochim. Acta,* vol. 37, pp. 2459-2465, 1992.

[5] B. Sun and M. Skyllas-Kazakos, "Chemical modification and electrochemical behaviour of graphite fibre in acidic vanadium solution," *Electrochim. Acta,* vol. 36, pp. 513-517, 1991.

[6] K. J. Kim, M.-S. Park, J.-H. Kim, U. Hwang, N. J. Lee, G. Jeong, *et al.*, "Novel catalytic effects of Mn_3O_4 for all vanadium redox flow batteries," *Chem. Commun.,* vol. 48, pp. 5455-5457, 2012.

[7] W. Wang and X. Wang, "Investigation of Ir-modified carbon felt as the positive electrode of an all-vanadium redox flow battery," *Electrochim. Acta,* vol. 52, pp. 6755-6762, 2007.

[8] D. J. Suárez, Z. González, C. Blanco, M. Granda, R. Menéndez, and R. Santamaría, "Graphite Felt Modified with Bismuth Nanoparticles as Negative Electrode in a Vanadium Redox Flow Battery," *ChemSusChem,* vol. 7, pp. 914-918, 2014.

[9] T.-M. Tseng, R.-H. Huang, C.-Y. Huang, K.-L. Hsueh, and F.-S. Shieu, "Improvement of titanium dioxide addition on carbon black composite for negative electrode in vanadium redox flow battery," *J. Electrochem. Soc.,* vol. 160, pp. A1269-A1275, 2013.

[10] B. Li, M. Gu, Z. Nie, X. Wei, C. Wang, V. Sprenkle, *et al.*, "Nanorod niobium oxide as powerful catalysts for an all vanadium redox flow battery," *Nano Lett.,* vol. 14, pp. 158-165, 2013.

[11] A. Bhattarai, N. Wai, R. Schweiss, A. Whitehead, T. M. Lim, and H. H. Hng, "Advanced porous electrodes with flow channels for vanadium redox flow battery," *Journal of Power Sources,* vol. 341, pp. 83-90, 2017.

[12] D. Aaron, Q. Liu, Z. Tang, G. Grim, A. Papandrew, A. Turhan, *et al.*, "Dramatic performance gains in vanadium redox flow batteries through modified cell architecture," *Journal of Power Sources,* vol. 206, pp. 450-453, 2012.

[13] T. D. Nguyen, A. Whitehead, G. G. Scherer, N. Wai, M. O. Oo, A. Bhattarai, *et al.*, "The oxidation of organic additives in the positive vanadium electrolyte and its effect on the performance of vanadium redox flow battery," *J. Power Sources,* vol. 334, pp. 94-103, 2016.

[14] A. Bhattarai, N. Wai, R. Schweiss, A. Whitehead, G. G. Scherer, P. C. Ghimire, *et al.*, "Study of flow behavior in all-vanadium redox flow battery using spatially resolved voltage distribution," *J. Power Sources,* vol. 360, pp. 443-452, 2017.

[15] S. Maeda, J. Sugawara, and H. Hayami, "Bipolar Plate for Redox Flow Battery," US20130037760 A1, 2011.

[16] S.-K. Park, J. Shim, J. H. Yang, C.-S. Jin, B. S. Lee, Y.-S. Lee, *et al.*, "The influence of compressed carbon felt electrodes on the performance of a vanadium redox flow battery," *Electrochim. Acta,* vol. 116, pp. 447-452, 1/10/ 2014.

[17] T.-C. Chang, J.-P. Zhang, and Y.-K. Fuh, "Electrical, mechanical and morphological properties of compressed carbon felt electrodes in vanadium redox flow battery," *J. Power Sources,* vol. 245, pp. 66-75, 2014.

[18] L. D. Brown, T. P. Neville, R. Jervis, T. J. Mason, P. R. Shearing, and D. J. Brett, "The effect of felt compression on the performance and pressure drop of all-vanadium redox flow batteries," *Journal of Energy Storage,* vol. 8, pp. 91-98, 2016.

[19] A. Shah, H. Al-Fetlawi, and F. Walsh, "Dynamic modelling of hydrogen evolution effects in the all-vanadium redox flow battery," *Electrochim. Acta,* vol. 55, pp. 1125-1139, 2010.

[20] K. Oh, S. Won, and H. Ju, "Numerical study of the effects of carbon felt electrode compression in all-vanadium redox flow batteries," *Electrochim. Acta,* vol. 181, pp. 13-23, 11/1/ 2015.

[21] A. Tang, J. Bao, and M. Skyllas-Kazacos, "Dynamic modelling of the effects of ion diffusion and side reactions on the capacity loss for vanadium redox flow battery," *J. Power Sources,* vol. 196, pp. 10737-10747, 2011.

[22] Graphite material and system-Speciality Graphites for Energy Storage, Datasheet, SGL Carbon, 2017, pp. 11.

[23] Redox-Flow-Batteries, Fumasep membrane types, Datasheet, Fumatech GmbH, pp. 4.

[24] K. Knehr and E. Kumbur, "Role of convection and related effects on species crossover and capacity loss in vanadium redox flow batteries," *Electrochem. Commun.,* vol. 23, pp. 76-79, 2012.